Multidomain Analysis and *n*th-Order Synchronous Reference Vector Adaptive Control of the Doubly Salient Motor

Yinfeng Hu, Lan Xiao, *Member, IEEE*, Chen Pan, Jinbo Li, *Student Member, IEEE*, and Chuyang Wang

***Abstract*—Due to the significant nonlinearity of the commutation of the square-wave current, the control of the doubly salient electromagnetic motor is hard to analyze quantitatively. This is because the present model is nonlinear and coupled. In this article, a linear decoupled model and symmetrical frequency shift cluster (SFSC) model are proposed based on a precise analysis of the time domain and complex-frequency domain. The results are extremely simple and mathematically computable. Moreover, these models focus on the average output torque, which is a key parameter at the same time. Furthermore, they explain well how torque ripple is generated. Based on the abovementioned results, a vector diagram of the harmonics of the phase current and inductance is proposed to precisely control the commutation in theory. Finally, *n*th-order synchronous reference vector adaptive control is proposed. The phase difference of each order is weighted to obtain the target function, which is proportional to the average output torque. The weighted phase difference is controlled adaptively to reach a maximum to realize the maximum torque per ampere. The theoretical results are verified by a 12/8 pole air-cooled prototype and related simulation and experimental results.**

***Index Terms*—Adaptive vector control, doubly salient electromagnetic motor (DSEM), frequency shift effect, linearization method.**

I. Introduction

THE doubly salient electromagnetic motor (DSEM) is a kind of nonsinusoidal electromagnetic machinery suitable for high-speed and harsh working environments [1]–[4]. The lack of windings in the rotor ensures the reliability of the DSEM in high-speed operation. Therefore, in the fields of aviation and electric vehicles, DSEMs have attracted attention as a special motor.

The excitation inductance of the DSEM is designed to change dramatically over a small region. In this way, the motor is fed by square-wave current that is easier to generate in high speed use than sinusoidal-wave current [5]. However, the commutation of the phase current consists of several states according to the control strategy, and is hard to calculate. Thus, the lack of an accurate theoretical calculation model of the motor itself influences the compensation and optimization in further steps.

For the modeling of nonsinusoidal motors, finite element analysis (FEA) is used to obtain the excitation inductance but the inductance model is nonlinear and cannot be used directly in control [6]. In [7], [8], numerical methods are used to model the nonlinear flux linkage function of the switched reluctance motor. However, the polynomial approximation requires sufficient terms to obtain acceptable accuracy, and this method is invalid for a wide working range when armature reaction is considered. In [9], a 4-D inductance model is built, showing that the armature reaction cannot be ignored when the model is built for some absolute value in a wide working range. In [10]–[12], intelligent learning approaches are applied, and the results are found to be precise for a wide working range, while the programming is relatively hard.

In summary, a new, precise, and valid model is needed for DSEM even when considering armature reaction. Ideally, this model is linear, simple, and easy to use.

For the control of the DSEM, various methods have been introduced [13]–[19]. Scholars have proposed advanced angle control (AAC) and their corresponding optimization methods [13]–[15]. By turning switches ON and OFF in advance to bring forward the commutation, AAC helps to decrease the torque loss in the commutation, but the values of the advanced angles are hard to determine. In the commutation, the circuit consists of multiple nonlinear time-varying elements and it is almost impossible to perform quantitative analysis directly in the time domain. However, the present studies are not sufficiently precise, because they are based on models deduced without considering the armature reaction or deduced based on approximate linearization.

In summary, a quantitative and precise optimization method that is unaffected by the armature reaction is needed for the DSEM. A simple and linear method is preferred.

To address the modeling and control problem, this article is organized as follows. In Section II, this article presents a Fourier FEA model of inductance and a linear decoupled model (LDM) in the time domain. In Section III, the Laplace transform is applied. The frequency shift effect and the SFSC model are

Manuscript received July 6, 2019; revised November 20, 2019; accepted January 20, 2020. Date of publication January 30, 2020; date of current version May 1, 2020. This work was supported by the National Natural Science Foundation of China under Award 51977108. Recommended for publication by Associate Editor J. Hur. *(Corresponding author: Lan Xiao.)*

Y. Hu, L. Xiao, and J. Li are with the Department of Automation Engineering, Nanjing University of Aeronautics and Astronautics, Nanjing 211106, China (e-mail: 1300214804@qq.com; xiaolan@nuaa.edu.cn; jinbo.l@foxmail.com).

C. Pan is with the Department of Electrical and Electronic Engineering, Huazhong University of Science and Technology, Wuhan 430074, China (e-mail: 912717707@qq.com).

C. Wang is with the College of Energy and Electrical Engineering, Hohai University, Nanjing 211106, China (e-mail: 792246001@qq.com).

Color versions of one or more of the figures in this article are available online at https://ieeexplore.ieee.org.

Digital Object Identifier 10.1109/TPEL.2020.2970459

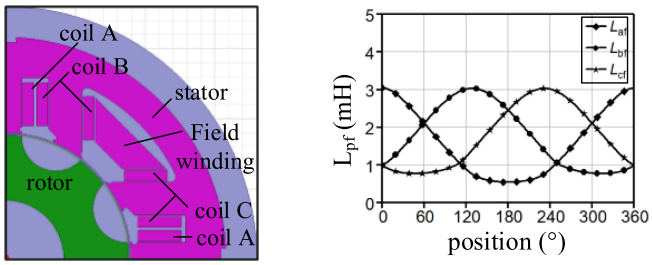

(a) (b)

Fig. 1. Nonlinear model of the DSEM.

TABLE I
FOURIER FEA MODEL OF EXCITATION INDUCTANCE

Harmonic Order	Magnitude(p.u.)	Phase
0	129%	
1	100%	90°
2	13.17%	90°
3	0.57%	90°
4	2.76%	90°
5	0.31%	90°
6	0.04%	90°
7	0.32%	90°
8	0.12%	270°

proposed in the complex-frequency domain. Then, the internal mechanism of how dc torque is generated is calculated theoretically. In Section IV, the composite self-optimization vector control is presented, which consists of current hysteresis control, AAC and frequency shift effect weighted (FSEW) algorithm. In Section V, the abovementioned theories are confirmed by relevant experiments and simulations.

II. LINEAR DECOUPLED MODEL

A. Fourier FEA Model

The FEA of the DSEM is obtained in MAXWELL as shown in Fig. 1(a), and the FEA results are given in Fig. 1(b). L_{pf} stands for the excitation inductance, and p represents phase A, B, and C. The waveform in Fig. 1 is neither sinusoidal nor linear. Because DSEM has a doubly salient structure and different pole-pair numbers of stators and rotors, the air gap is uneven. Therefore, under dc current excitation, the excitation inductance is nonsinusoidal. Fourier series decomposition is applied to the results of FEA in this article and the Fourier series of L_{pf} are obtained as follows. Mathematical analysis results of the prototype are shown in Table I. L_{pfn} stands for the nth harmonic component of the excitation inductance, N_{p} stands for the pole-pair number, and θ stands for the position of the rotor

$$\begin{cases} L_{\mathrm{af}} = \sum_{\mathrm{n}=1}^{+\infty} L_{\mathrm{afn}} \sin\left[\mathrm{n}N_{\mathrm{p}}\left(\theta_{\mathrm{n}} + \dfrac{\pi}{2}\right)\right] \\ L_{\mathrm{bf}} = \sum_{\mathrm{n}=1}^{+\infty} L_{\mathrm{bfn}} \sin\left[\mathrm{n}N_{\mathrm{p}}\left(\theta_{\mathrm{n}} - \dfrac{\pi}{6}\right)\right] \\ L_{\mathrm{cf}} = \sum_{\mathrm{n}=1}^{+\infty} L_{\mathrm{cfn}} \sin\left[\mathrm{n}N_{\mathrm{p}}\left(\theta_{\mathrm{n}} - \dfrac{5\pi}{6}\right)\right] \end{cases} \tag{1}$$

$$\begin{cases} \dfrac{\partial L_{\mathrm{af}}}{\partial\theta} = -\sum_{\mathrm{n}=1}^{+\infty} \mathrm{n}N_{\mathrm{p}} L_{\mathrm{afn}} \sin\left(\mathrm{n}N_{\mathrm{p}}\theta_{\mathrm{n}}\right) \\ \dfrac{\partial L_{\mathrm{bf}}}{\partial\theta} = -\sum_{\mathrm{n}=1}^{+\infty} \mathrm{n}N_{\mathrm{p}} L_{\mathrm{bfn}} \sin\left[\mathrm{n}N_{\mathrm{p}}\left(\theta_{\mathrm{n}} - \dfrac{2\pi}{3}\right)\right] \\ \dfrac{\partial L_{\mathrm{cf}}}{\partial\theta} = -\sum_{\mathrm{n}=1}^{+\infty} \mathrm{n}N_{\mathrm{p}} L_{\mathrm{cfn}} \sin\left[\mathrm{n}N_{\mathrm{p}}\left(\theta_{\mathrm{n}} + \dfrac{2\pi}{3}\right)\right]. \end{cases} \tag{2}$$

B. Coupling of the Fourier FEA Model

The FEA results of L_{pf} are nonlinear and cannot be linearized directly. However, L_{pf} itself is not of particular interest, the focus is how to control the current to produce torque. As described in [1], the output torque per phase can be expressed as

$$T_{\mathrm{p}} = T_{\mathrm{pr}} + T_{\mathrm{pe}} = \frac{1}{2} i_{\mathrm{p}}^2 \frac{\partial L_{rmp}}{\partial\theta} + I_{\mathrm{f}} i_{\mathrm{p}} \frac{\partial L_{\mathrm{pf}}}{\partial\theta} \tag{3}$$

where T_{pr} stands for the reluctance torque, T_{pe} stands for the excitation torque, L_{p} stands for the self-inductance per phase, and i_{p} stands for the phase current. Because T_{pr} is relatively small, so T_{pr} can be neglected [1]. Then, total output torque that contains only excitation torque can be expressed as

$$T = T_{\mathrm{a}} + T_{\mathrm{b}} + T_{\mathrm{c}} = I_{\mathrm{f}} \left(i_a \frac{\partial L_{\mathrm{af}}}{\partial\theta} + i_{\mathrm{b}} \frac{\partial L_{\mathrm{bf}}}{\partial\theta} + i_{\mathrm{c}} \frac{\partial L_{\mathrm{cf}}}{\partial\theta} \right). \tag{4}$$

Similarly, the phase current can be expressed as

$$\begin{cases} i_{\mathrm{a}} = \sum_{m=1}^{+\infty} I_{\mathrm{m}} \sin\left(\mathrm{m}N_{\mathrm{p}}\theta_{\mathrm{n}} + \Delta\theta_{\mathrm{m}}\right) \\ i_{\mathrm{b}} = \sum_{m=1}^{+\infty} I_{\mathrm{m}} \sin\left[\mathrm{m}N_{\mathrm{p}}(\theta_{\mathrm{n}} - \dfrac{2\pi}{3}) + \Delta\theta_{\mathrm{m}}\right] \\ i_{\mathrm{c}} = \sum_{\mathrm{m}=1}^{+\infty} I_{\mathrm{m}} \sin\left[\mathrm{m}N_{\mathrm{p}}\left(\theta_{\mathrm{n}} + \dfrac{2\pi}{3}\right) + \Delta\theta_{\mathrm{m}}\right] \end{cases} \tag{5}$$

where $\Delta\theta_{\mathrm{m}}$ stands for the initial phase of the mth harmonic of the phase current. By substituting (2) and (5) into (4), we obtain

$$\begin{aligned} T &= T_a + T_b + T_c = T_{\mathrm{dc}} + T_{\mathrm{ac}} \\ &= -\sum_{\mathrm{m}=1}^{+\infty}\sum_{\mathrm{n}=1}^{+\infty} I_{\mathrm{f}} I_{\mathrm{m}} \mathrm{n}N_{\mathrm{p}} L_{\mathrm{afn}} \\ &\quad \sin(\mathrm{n}N_{\mathrm{p}}\theta_{\mathrm{n}}) \sin[\mathrm{m}N_{\mathrm{p}}\theta_{\mathrm{n}} + \Delta\theta_{\mathrm{m}}] \\ &\quad - \sum_{\mathrm{m}=1}^{+\infty}\sum_{\mathrm{n}=1}^{+\infty} I_{\mathrm{f}} I_{\mathrm{m}} n N_{\mathrm{p}} L_{\mathrm{bfn}} \\ &\quad \times \sin\left[\mathrm{n}N_{\mathrm{p}}\left(\theta_{\mathrm{n}} - \frac{2\pi}{3}\right)\right] \sin\left[\mathrm{m}N_{\mathrm{p}}\left(\theta_{\mathrm{n}} - \frac{2\pi}{3}\right) + \Delta\theta_{\mathrm{m}}\right] \\ &\quad - \sum_{\mathrm{m}=1}^{+\infty}\sum_{\mathrm{n}=1}^{+\infty} I_f I_{\mathrm{m}} n N_{\mathrm{p}} L_{\mathrm{cfn}} \\ &\quad \times \sin\left[\mathrm{n}N_{\mathrm{p}}\left(\theta_{\mathrm{n}} + \frac{2\pi}{3}\right)\right] \sin\left[\mathrm{m}N_{\mathrm{p}}\left(\theta_{\mathrm{n}} + \frac{2\pi}{3}\right) + \Delta\theta_{\mathrm{m}}\right] \end{aligned} \tag{6}$$

where $T_{\rm dc}$ represents the average component of the output torque, and $T_{\rm ac}$ represents the ac component of the output torque. We define (6) as the Fourier FEA model of the DSEM.

We know the following trigonometric formula

$$\sin\omega_1 t\cdot\sin(\omega_2 t+\Delta\theta) = -\frac{[\cos(\omega_1 t+\omega_2 t+\Delta\theta)-\cos(\omega_1 t-\omega_2 t-\Delta\theta)]}{2} \quad (7)$$

where ω_1, ω_2, and $\Delta\theta$, are random numbers. The results consist of two terms. A high-frequency component and a low-frequency component. When $\omega_1 \neq \omega_2$, the product consists of two ac components. When $\omega_1 = \omega_2$, the product consists of a second harmonic of ω_1 and a dc component.

The situation is the same as that in (6). It is complex to write out the relationship completely for every pair. However, by considering the frequency information of the multiplication term, we can still draw the conclusion that each term in (6) actually contains two parts. The dc component and the ac component. The dc component is generated by the current and excitation inductance change rate (EICR) of the same order.

From the abovementioned analysis, we can see that there is complex coupling between the EICR and the phase current of different orders. The Fourier FEA model expresses the instantaneous torque, and is still nonlinear.

To suppress torque ripple quantitively, methods should be proposed in the following two ways. First, decrease the multiplication of different orders; for example, control the phase difference between the second harmonic current and first EICR to be 90°, which lets the multiplication to be zero. Second, decrease the main harmonic components of the current. Note that these methods trade off the dc output torque to decrease the torque ripple.

C. Linear Decoupled Model

Performing the Park transformation with a permanent magnet synchronous motor can decouple three phase voltages of the same frequency. Similarly, we interpret the EICR as Park transformation and the phase current as the voltage in the abovementioned example, and LDM could be achieved by applying Park transformation of one frequency at one time. For example, if we wish to decouple the fundamental phase current component, setting $n = 1$ in (6), we obtain

$$\begin{aligned}
T &= T_a + T_b + T_c = T_{\rm dc1} + T_{\rm dc}{}' + T_{\rm ac} \\
&= -\sum_{\rm m=1}^{+\infty}\sum_{\rm n=2}^{+\infty} I_{\rm f} I_{\rm m} n N_{\rm p} L_{\rm afn} \sin({\rm n}N_{\rm p}\theta_{\rm n})\sin[{\rm m}N_{\rm p}\theta_{\rm n}+\Delta\theta_{\rm m}] \\
&\quad -\sum_{\rm m=1}^{+\infty}\sum_{\rm n=2}^{+\infty} I_{\rm f} I_{\rm m} n N_{\rm p} L_{\rm bfn} \sin\left[{\rm n}N_{\rm p}\left(\theta_{\rm n}-\frac{2\pi}{3}\right)\right] \\
&\quad \times \sin\left[{\rm m}N_{\rm p}\left(\theta_{\rm n}-\frac{2\pi}{3}\right)+\Delta\theta_{\rm m}\right] \\
&\quad -\sum_{m=1}^{+\infty}\sum_{\rm n=2}^{+\infty} I_{\rm f} I_{\rm m} n N_{\rm p} L_{\rm cfn} \sin\left[{\rm n}N_{\rm p}\left(\theta_{\rm n}+\frac{2\pi}{3}\right)\right] \\
&\quad \times \sin\left[{\rm m}N_{\rm p}\left(\theta_{\rm n}+\frac{2\pi}{3}\right)+\Delta\theta_{\rm m}\right] \\
&\quad -\sum_{\rm m=2}^{+\infty} I_{\rm f} I_{\rm m} n N_{\rm p} L_{\rm af1} \sin(N_{\rm p}\theta_{\rm n})\sin[mN_{\rm p}\theta_{\rm n}+\Delta\theta_{\rm m}] \\
&\quad -\sum_{\rm m=2}^{+\infty} I_{\rm f} I_{\rm m} n N_{\rm p} L_{bf1} \sin\left[N_{\rm p}\left(\theta_{\rm n}-\frac{2\pi}{3}\right)\right] \\
&\quad \times \sin\left[{\rm m}N_{\rm p}\left(\theta_{\rm n}-\frac{2\pi}{3}\right)+\Delta\theta_{\rm m}\right] \\
&\quad -\sum_{\rm m=2}^{+\infty} I_{\rm f} I_{\rm m} n N_{\rm p} L_{\rm cf1} \sin\left[N_{\rm p}(\theta_{\rm n}+\frac{2\pi}{3})\right] \\
&\quad \times \sin\left[{\rm m}N_{\rm p}\left(\theta_{\rm n}+\frac{2\pi}{3}\right)+\Delta\theta_{\rm m}\right] \\
&\quad -\frac{3}{2} I_{\rm f} I_1 N_{\rm p} L_{\rm af1}\cos(\Delta\theta_1 N_{\rm p}) \qquad (8)
\end{aligned}$$

where $\rm T_{dc1}$ stands for the average output torque generated by the fundamental phase current component and $\rm T_{dc}{}'$ is the dc torque generated by the harmonics of the EICR except first one. Theoretically, an LDM of any order, denoted as LDM-n, can be obtained. The LDM-1 in the time domain is obtained as

$$T_{\rm dc1} = -\frac{3}{2} I_{\rm f} I_1 N_{\rm p} L_{\rm af1}\cos(\Delta\theta_1). \quad (9)$$

This linearizes the nonlinear Fourier FEA model and expresses the relation between the average output torque and the phase current. The sum of LDM is

$$T_{\rm dc} = \frac{3}{2}\sum_{\rm n=1}^{+\infty} I_{\rm f} I_1 n N_{\rm p} L_{\rm afn}\cos(\Delta\theta_{\rm n}). \quad (10)$$

III. SFSC Model

A. Frequency Shift Effect

By applying the Park transformation to the Fourier FEA model, relation between the average output torque and the phase current is described as the LDM. LDM is quite simple; however, it fails to demonstrate the coupling of abovementioned three situations, which is the main cause for ac output torque or torque ripple in our nomenclature. To establish a model that contains all the coupling information, frequency domain analysis is necessary. To make this analysis simple, we rewrite the Fourier FEA model as

$$\begin{aligned}
T = &-I_{\rm f} i_{\rm a}\theta\left[\sum_{\rm n=1}^{+\infty} {\rm n}N_{\rm p} L_{\rm afn}\sin({\rm n}N_{\rm p}\theta)\right. \\
&-I_{\rm f} i_{\rm a}\left(\theta-\frac{2\pi}{3}\right)\left[\sum_{\rm n=1}^{+\infty} {\rm n}N_{\rm p} L_{\rm bfn}\sin\left[{\rm n}N_{\rm p}\left(\theta-\frac{2\pi}{3}\right)\right]\right. \\
&-I_{\rm f} i_{\rm a}\left(\theta+\frac{2\pi}{3}\right)\left[\sum_{\rm n=1}^{+\infty} {\rm n}N_{\rm p} L_{\rm cfn}\sin\left[{\rm n}N_{\rm p}\left(\theta+\frac{2\pi}{3}\right)\right]\right]. \qquad (11)
\end{aligned}$$

TABLE II
FREQUENCY COMPONENT OF OUTPUT TORQUE

Current Frequency	Frequency Shift	Torque Frequency
dc	$\pm f_1$	f_1
		$-f_1$
f_1	$\pm f_1$	dc
		$2f_1$
$2f_1$	$\pm f_1$	$3f_1$
		f_1
dc	$\pm 2f_1$	$2f_1$
		$-2f_1$
f_1	$\pm 2f_1$	$3f_1$
		$-f_1$
$2f_1$	$\pm 2f_1$	$4f_1$
		dc

Laplace transformations are applied to the Fourier FEA model, and the result in the complex domain is

$$T(s) = -\frac{\mathrm{j}}{2} I_{\mathrm{f}} N_{\mathrm{p}} \left(1 + e^{-\frac{2\pi}{3}\mathrm{s}} + e^{\frac{2\pi}{3}\mathrm{s}}\right) \times \left\{ \sum_{n=1}^{+\infty} \mathrm{n} L_{\mathrm{pfn}} \left[I\left(s + j\mathrm{n} N_{\mathrm{p}} 2\pi f_{\mathrm{mec}}\right) - I\left(s - j\mathrm{n} N_{\mathrm{p}} 2\pi f_{\mathrm{mec}}\right) \right] \right\}. \quad (12)$$

This is a complex-frequency domain model of the output torque and the phase current. Because the model expresses the nonlinearity of the EICR in a concise way, it is possible to analytically calculate the output torque when the phase current can be measured.

From the abovementioned results, two conclusions can be drawn. First, the cause of the *n*th-order output torque can be described quantitatively. For example, the output torque fundamental component is generated by the dc current, the fundamental component of the current, and the second-order component of the current and so on. The quantificational expression can be easily obtained by setting $\mathrm{s} = \mathrm{j}\omega$. Second, the effect of the phase current is described. For example, the fundamental component of the phase current generates an output torque of the second harmonic order, and dc, third and first harmonic orders, and so on. This kind of phenomenon is defined as the frequency shift effect.

B. SFSC Model

To describe the complex couplings, an SFSC model is introduced, as shown in Table II.

As the abovementioned table shows, one frequency of the phase current can generate a cluster of frequencies of the output torque after nonlinear inductance. The fundamental component of the phase current can be shifted in frequency symmetrically for $\pm f$, $\pm 2f$, and so on, thus, generating output torques of dc, $2f$, $-f$, $3f$, and so on. The results are for a single phase, however if three phases are considered, the torque harmonics that are not the third or multiples of the third will offset each other. The SFSC model not only reveals the mechanism by which the average or ac torque is generated, but also helps to explain the amplitude–frequency characteristic.

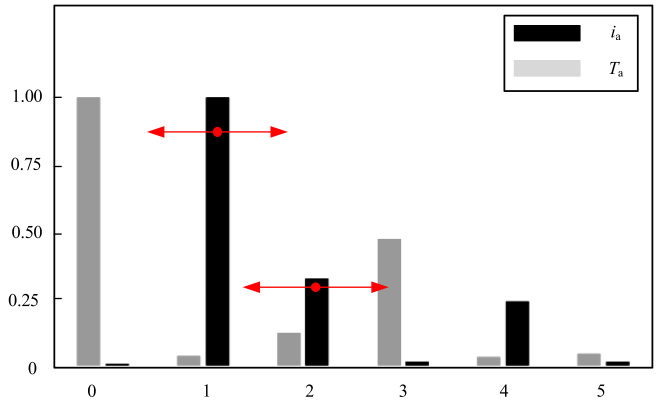

Fig. 2. FFT results of the phase current and output torque.

As shown in Fig. 2, the fast Fourier transform (FFT) is applied to the phase-current waveform and output-torque waveform obtained in the simulation. The main components of the phase A current do not include harmonics of the third order or multiples of the third order and by Table I, the strongest frequency shift effect is by the first order. So, the main components of the output torque can be dc, and the second and third harmonics. Considering that the amplitude of the output torque could be nonzero only when the order takes integer times of three or multiples of three on the condition of three-phase symmetry, the main orders of the harmonics of the output torque are three and nine. The FFT results of the simulation are as follows, and the components are mainly dc and the third and ninth harmonic orders. Due to the offset effect of three-phase symmetry, the amplitudes of lower-order harmonics such as the first or second are small instead.

In summary, SFSC model explains how torque ripple is generated. First, there exist strong enough harmonics of the phase current and harmonics of the EIRC, and their orders are adjacent. Second, the orders of harmonics of torque take integer times of three or multiples of three.

C. Similarities and Differences With the LDM

By setting $s = 0$, the average output torque can be written as the sum of

$$T(0) = -\frac{j3}{2} I_{\mathrm{f}} N_{\mathrm{p}} \left\{ \sum_{n=1}^{+\infty} n L_{\mathrm{pfn}} \left[I(j\mathrm{n} N_{\mathrm{p}} 2\pi f_{\mathrm{mec}}) - I\left(-j\mathrm{n} N_{\mathrm{p}} 2\pi f_{\mathrm{mec}}\right) \right] \right\}. \quad (13)$$

Inserting (5) into (12), we obtain

$$T(0) = -\frac{j3}{2} I_{\mathrm{f}} N_{\mathrm{p}} \sum_{n=1}^{+\infty} \mathrm{n} L_{\mathrm{pfn}} I_{\mathrm{n}} \cos\theta_{\mathrm{m}}. \quad (14)$$

For the ease of comparison, all the symbols in (13) are the same as in (9). The expression is in consistent with the results of the LDM deduced in the time domain.

In the frequency domain, we take the output torque harmonic of order of third as an example. Setting s = j3ω, we obtain

$$T(s) = -\frac{j3}{2} I_{\mathrm{f}} N_{\mathrm{p}} \left\{ \sum_{n=1}^{+\infty} nL_{\mathrm{pfn}} [I\left(j(\mathrm{n}+3)N_{\mathrm{p}} 2\pi f_{\mathrm{mec}}\right) - I\left(j\left(3-\mathrm{n}\right)N_{\mathrm{p}} 2\pi f_{\mathrm{mec}}\right)] \right\}. \quad (15)$$

This shows the magnitude and phase relations between the torque and some harmonic of the phase current. Note that although the SFSC model is more complex than other models, it is more suitable for the analysis of frequency and has the clear and detailed information about the coupling and phase reserved.

IV. *N*TH SYNCHRONOUS REFERENCE VECTOR CONTROL

A. *Weighted Phase Difference*

Based on the analysis of the SFSC model and the LDM in the multidomain, we define the FSEW phase difference as

$$\bar{\theta} = \sum_{n=1}^{k} \frac{\mathrm{n} L_{\mathrm{pfn}} I_{\mathrm{n}} \cos(\Delta\theta_{\mathrm{n}})}{I_{\mathrm{rms}}} \quad (16)$$

where L_{pfn} is the harmonic excitation inductance. The weighted phase difference is defined to increase the average output torque. The physical significance of the weighted phase difference is deduced as

$$\frac{T_{\mathrm{dc}}}{I_{\mathrm{rms}}} = -\frac{3 I_{\mathrm{f}} N_{\mathrm{p}}}{2} \bar{\theta}. \quad (17)$$

This ratio is proportional to the torque/current ratio.

The fundamental frequency can be as high as 1.3 kHz when the rotation speed is 10 000 r/min. Therefore, it is almost impossible to produce a nonlinear phase current wave as with the EICR to let the phase difference be zero for each order. To achieve the maximum torque per ampere (MTPA), a weighted phase difference is introduced. Thus, how large the phase difference is between some phase current harmonic and some EICR harmonics should be specified under the condition that weighs the phased difference to be maximum. The following section presents how to realize the MTPA with weighted phase difference as the target function.

Note that, for other nonsinusoidal motors, similar analysis and control can be applied as well to realize quantitative modeling, control and optimization.

B. *Vector Control of the* n*th Synchronous Reference Frame*

The flow diagram of self-optimization is shown in Fig. 3.

In the control program, harmonic detection is always running. The Boolean value of the conditional statement is always "true". Thus, information about the amplitude and phase of each harmonic can be obtained promptly.

The main control algorithm consists of three parts. First, a counter sets the value of the wait periodically. This part is easy and simple, so it is omitted here. Second, when the value of the wait is reached, the algorithm begins the next step to weight the phase and amplitude of harmonics to obtain the weighted phase according to (16). Third, the perturbation-observation method works to find the value of the advanced angle, which allows the target function in (16) to be maximized.

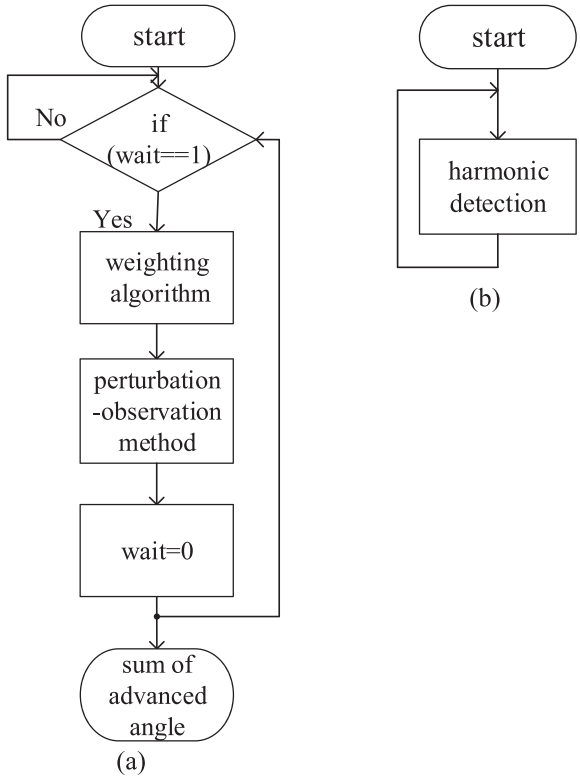

Fig. 3. Flow diagram of the self-optimization process.

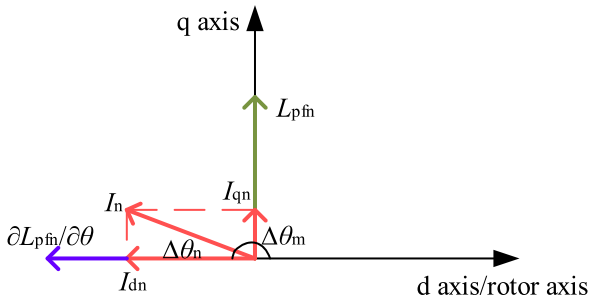

Fig. 4. Definition of the synchronous reference frame of some order.

In the synchronous reference frame of some order, $\Delta\theta_{\mathrm{n}}$ as mentioned earlier is defined in Fig. 4. The *d*-axis serves as the reference of the electric angle of some order and the rotor axis of some order. In this way, the DSEM can be decomposed into *n* permanent magnet synchronous motors with rotation speeds of actual speed, which is two times the actual speed and so on. Thus, the phase difference defined earlier is similar to the angle between the back electromotive force and current vector in synchronous motor control. The definition is shown in Fig. 4.

TABLE III
MEANINGS OF THE SYMBOL USED IN THIS ARTICLE

Symbol	Meaning	Location
θn	d axis of some order When n=1, it equals to the mechanical position of the rotor	equation 1 equation 2
$\Delta\theta$m	phase difference between the phase current and the d axis of some order	equation 5 equation 6
$\Delta\theta$n	complement of $\Delta\theta$m for consistency with the simulation results	equation 14 equation 16

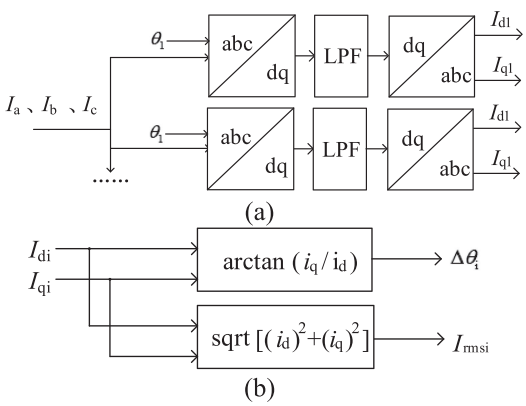

Fig. 5. Harmonic detection algorithm.

For improved understanding, Table III gives the definition of the symbol of the angles used.

Synchronous reference frame harmonic detection is introduced here to obtain the magnitude and phase of each order of harmonics. The schema of the algorithm is shown in Fig. 5.

The algorithm contains three main steps. First, sample the phase current, apply the Park transformation of the corresponding order, filter the low-frequency components and apply the inverse transformation, which is carried out at the frequency of the sampling interruption. Second, the results of the first step are weighted and the weighted phase difference is calculated per 100 ms, which reduces the demand on the central processing unit. Third, adaptive control is applied.

To better filter the ac component, a moving average filter (MAF) is used here. The filter is analyzed in [12], and the Bode diagram is shown in Fig. 6. Because n_{ref} is set as 10 000 r/min, the electric frequency of the fundamental is 1.33 kHz. The number of sample points is set as 50, so here we choose the sampling frequency to be 66.5 kHz.

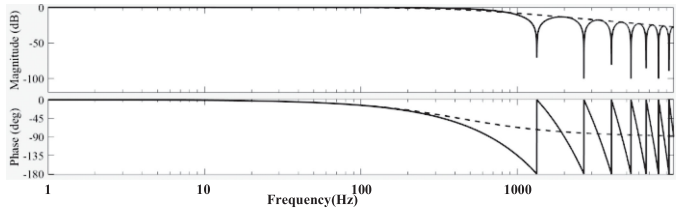

Fig. 6. Bode diagram of MAF.

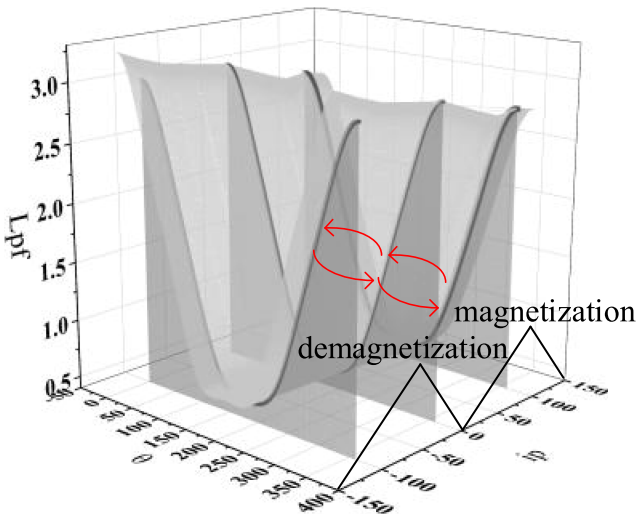

Fig. 7. Effect of armature reaction on excitation inductance.

C. Effect of the Armature Reaction on Proposed Optimization Method

As shown in Fig. 7, the armature reaction can dramatically affect the value of L_{pf} [20]. The negative current acts as demagnetization and L_{pf} increases while the positive one acts as magnetization and L_{pf} decreases. Considering the saturation of magnet material, the increment is larger than the decrement.

When phase current turns from positive to negative periodically, the excitation inductance becomes smaller and larger periodically as the red arrow shows.

However, the armature reaction for a nonsinusoidal motor is hard to calculate precisely; so here, we present a qualitative error analysis.

First, rewrite (16) and (17) in the following form:

$$\frac{T_{dc}}{I_{rms}} = -\frac{3I_f N_p}{2}\sum_{n=1}^{k}\frac{nL_{pfn}I_n\cos(\Delta\theta_n)}{I_{rms}}. \quad (18)$$

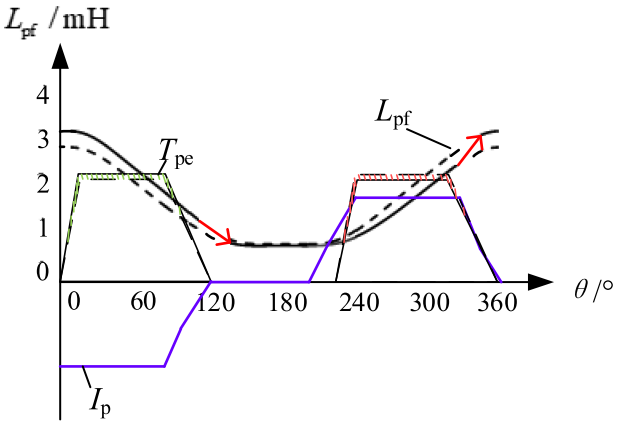

Fig. 8. Waveforms of the excitation inductance and the phase current of the single phase considering armature reaction.

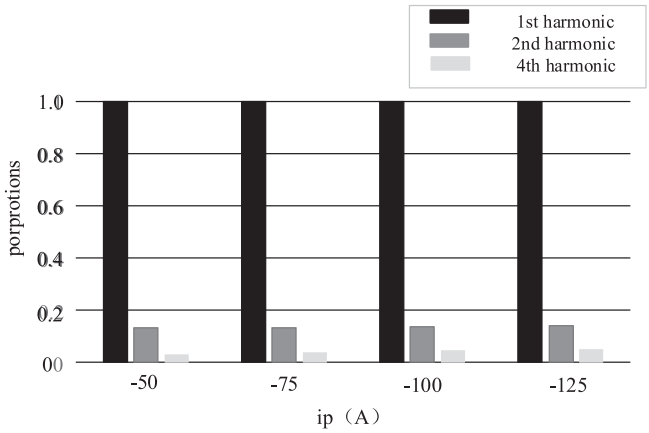

Fig. 9. FFT results of excitation inductance with different armature reaction.

When considering the armature reaction, (18) assumes the following form:

$$\frac{T_{\rm dc}}{I_{\rm rms}} = -\frac{3I_{\rm f}N_{\rm p}}{2}\sum_{n=1}^{k}\frac{{\rm n}\left(L_{\rm pfn}+\Delta L_{\rm pfn}\right)I_{\rm n}\cos\left(\Delta\theta_{\rm n}\right)}{I_{\rm rms}} \quad (19)$$

$$\frac{T_{\rm dc}}{I_{\rm rms}} = -\frac{3I_{\rm f}N_{\rm p}}{2}\sum_{n=1}^{k}\frac{{\rm n}(L_{\rm pfn}-\Delta L_{\rm pfn}{}')I_{\rm n}\cos(\Delta\theta_{\rm n})}{I_{\rm rms}}. \quad (20)$$

where $+\Delta{\rm L}_{\rm pfn}(i_{\rm p},I_{\rm f},\theta)$ is the increment of the excitation inductance when the phase current is negative, and $-\Delta{\rm L}_{\rm pfn}$ $(i_{\rm p},I_{\rm f},\theta)$ is the decrement of the excitation inductance when the phase current is positive. The equation shows the instantaneous value of the ratio of torque to current. Therefore, the average of ratio of torque to current is

$$\int_{T_s}\frac{T_{\rm dc}/I_{\rm rms}}{T_s}dt = -\frac{3I_{\rm f}N_{\rm p}}{2I_{\rm rms}T_s} \times\left[\int_0^{T_s/2}\sum_{n=1}^{k}\frac{{\rm n}(L_{\rm pfn}+\Delta L_{\rm pfn})I_{\rm n}\cos(\Delta\theta_{\rm n})}{I_{\rm rms}}dt + \int_0^{T_s/2}\sum_{n=1}^{k}\frac{{\rm n}(L_{\rm pfn}-\Delta L_{\rm pfn}{}')I_{\rm n}\cos(\Delta\theta_{\rm n})}{I_{\rm rms}}dt\right]. \quad (21)$$

Considering the symmetry of the control, for ideal motor model, we have

$$\Delta L_{\rm pfn} = \Delta L_{\rm pfn}{}'. \quad (22)$$

The abovementioned analysis can be explained in the Fig. 8. The solid line is for the actual value of the excitation inductance. The dashed line is drawn for comparison. The red shadowed part is the loss of torque because of the armature reaction, and the green one is the gain. Ideally, they offset each other in the proposed optimization method. In this way, the proposed method obtains the dc output torque, avoiding the precise calculation of the effect of armature reaction.

When saturation of magnetic material is considered, the error sources of this optimization method are obtained mainly from the two aspects.

First, when saturation of magnetic material is considered, $\Delta{\rm L}_{\rm pfn}$ and $\Delta{\rm L}_{\rm pfn}{}'$ cannot offset each other completely and causes the error. Nevertheless, the error decreases. The situation is shown in Fig. 8.

In this situation, considering the positive term and the negative term cannot offset each other completely, we use a constant bias to simplify the effect of the armature reaction, which satisfies

$$\left[\int_0^{T_s/2}\sum_{n=1}^{k}\frac{{\rm n}(L_{\rm pfn}+\Delta L_{\rm pfn})I_{\rm n}cos(\Delta\theta_{\rm n})}{I_{\rm rms}}dt + \int_0^{T_s/2}\sum_{n=1}^{k}\frac{{\rm n}(L_{\rm pfn}-\Delta L_{\rm pfn}{}')I_{\rm n}\cos(\Delta\theta_{\rm n})}{I_{\rm rms}}dt\right] = \int_0^{T_s}\sum_{n=1}^{k}{\rm n}L_{\rm pfn}{}'I_{\rm n}\cos(\Delta\theta_{\rm n})dt. \quad (23)$$

We call $L_{\rm pfn}{}'$ the equivalent inductance here. Obviously, $L_{\rm pfn}{}'$ is larger than $L_{\rm pfn}$, identical to the negative phase current situation in the literature [20]. To decrease the error, we use $L_{\rm pfn}{}'$ in the FEA when the load current is negative.

Second, $L_{\rm pfn}{}'$ changes as the load changes. When load changes, the equivalent inductance $L_{\rm pfn}{}'$ changes, too. Therefore, the weighting factors programmed in advance may not represent the actual inductance.

The FEA results of the armature reaction are shown in Fig. 9. The conclusion can be drawn that although the absolute value of the inductance changes, the proportions of the main harmonics generating the dc output torque stay almost the same as the phase current changes. This means that the optimization is still valid because the weighting coefficients are influenced by the proportions of the different orders of the harmonics.

The main harmonics are considered to be the first and second harmonics. The waveforms become sharp when armature reaction acts as demagnetization mainly because the fourth harmonic grows larger. The results are shown in Fig. 9.

In Fig. 9 we use the standard value. The base value is the first harmonic of each order.

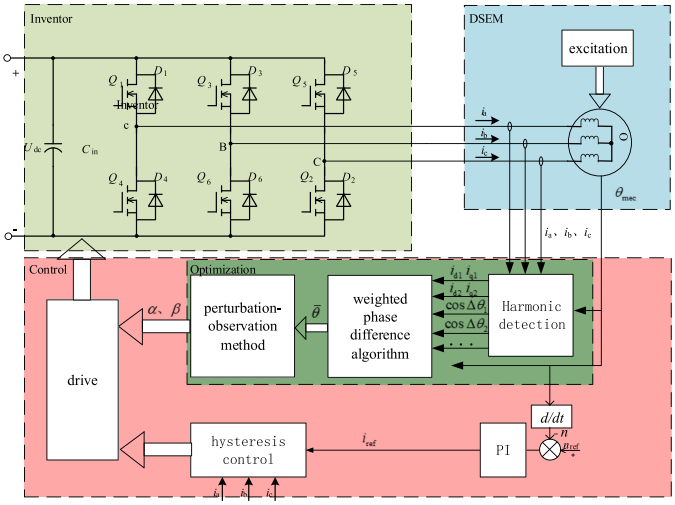

Fig. 10. Diagram of the new control system.

Thus, when the DSEM works under a certain condition, the effect of the armature reaction on the proposed optimization method is undermined. When the load changes dramatically, (18) is still valid because the weighting coefficients that are influenced by the proportions of the harmonics are almost constant.

D. Local Optimum and Vibration

To ensure that there exists no local optimum problem, optimization starts at the lowest limit of the sum of α and β and then restarts at the highest limit of the sum of α and β. In practice, no local optimum is found.

For the case of vibration, the step is set proportional to the weighted phase difference, and the step therefore decreases over time. Ultimately, the sum of α and β changes in a very small range as a response to the continuous fluctuation in the rotation speed.

V. Experiment and Simulation Verification

As shown in Fig. 10, the motor is controlled by speed outer loop and current hysteresis loop. The nonlinear FEA model built in MAXWELL is exported and a lookup table is used to build up a nonlinear model in MATLAB for simulation. The control is programmed in the S-function model to keep consistent with reality as much as possible. The results obtained online are shown in Fig. 11. The solid line is fundamental, the dash line is the second harmonic and the dotted dash line is the fourth harmonic, which are the main sources of the output torque by the forthcoming analysis. The FSEW phase difference changes as the advance angle changes and reaches a higher value finally.

In experiments, the results of adaptive control are shown in Figs. 12–17. Experimental conditions are $n_{\mathrm{ref}} = 10\,000$ r/min, and $I_{\mathrm{f}} = 7$ A.

From the abovementioned results, when U/ω increases, the commutation is easier. Therefore, the commutation does not need that much value of the advanced angle, and the ideal advanced parameters decrease. When the phase current increases,

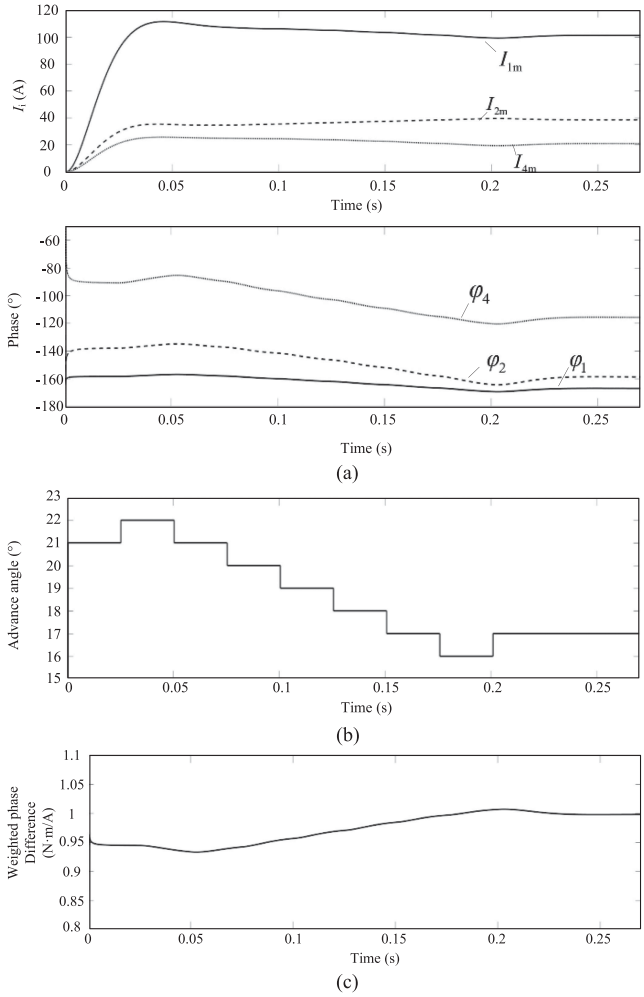

Fig. 11. Simulation results. (a) Phase differences and amplitudes of the first, second, and fourth phase currents obtained by harmonic detection. (b) Dynamics of the startup and self-optimization process. (c) Dynamics of the observed ratio of torque to current. Condition: $n_{\mathrm{ref}} = 10\,000$ r/min, $U_{\mathrm{dc}} = 200$ V, $T_{\mathrm{load}} = 9.5$ N·m, $U/\omega = 0.2$V·s/rad.

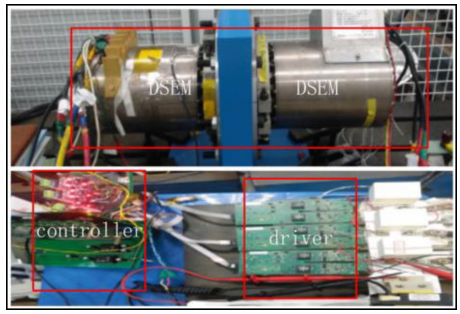

Fig. 12. Experiment platform of the DSEM.

more time is need for the phase current to reach a higher value, and thus ideal advanced angle parameters increase

$$\mathrm{ratio} = \frac{N_{\mathrm{sample}} 2^{N_{\mathrm{position}}}}{360 \cdot N_{\mathrm{p}}} = 2.84 \tag{24}$$

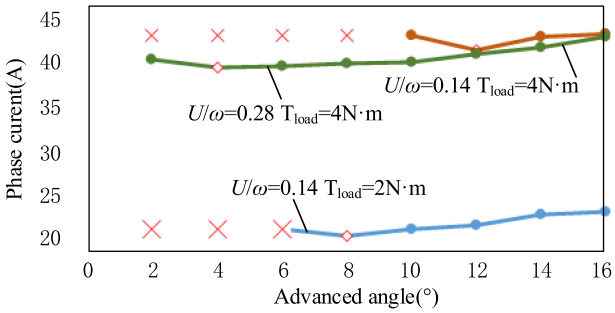

Fig. 13. Simulation of the root mean square value of the phase current when the advance angle changes (Solid line: $n_{\mathrm{ref}} = 10\,000$ r/min, $U_{\mathrm{dc}} = 150$ V, and $T_{\mathrm{load}} = 4$ N·m. Dashed line: $n_{\mathrm{ref}} = 5000$ r/min, $U_{\mathrm{dc}} = 150$ V, and $T_{\mathrm{load}} = 4$ N·m. Dotted line: $n_{\mathrm{ref}} = 10\,000$ r/min, $U_{\mathrm{dc}} = 150$ V, and $T_{\mathrm{load}} = 2$ N·m.). The cross in the figure stands for the situation that the output torque cannot be generated because of unreasonable advanced angle parameters. The diamond stands for the advanced angle parameters the adaptive method finds.

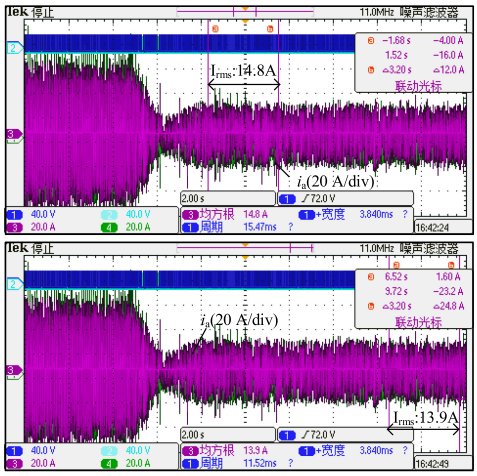

(a)

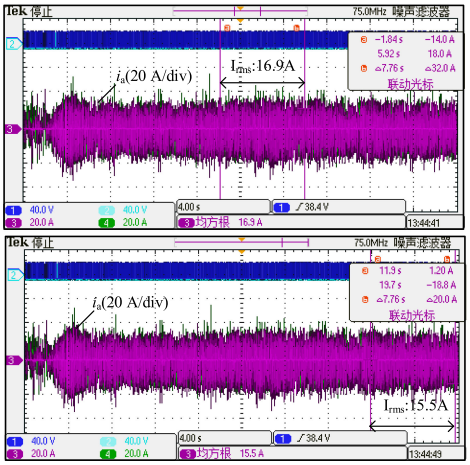

(b)

Fig. 14. Load step-up and step-down under the conditions of $I_{\mathrm{f}} = 3$ A, $U_{\mathrm{dc}} = 45$ V, and $n_{\mathrm{ref}} = 5000$ r/min. (a) Output power step-down from 2 to 1 kW. (b) Output power step-up from 0.5 to 1 kW.

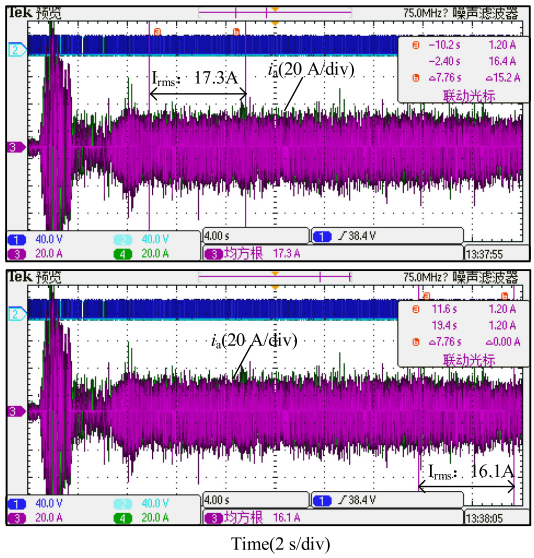

Fig. 15. Dynamics of the startup and self-optimization process.

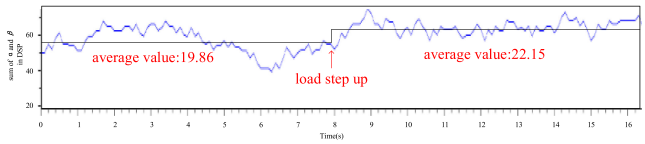

Fig. 16. Advance angle tuned by FSEW self-optimization during load-up dynamics. The ratio of the signal value to the actual value of advanced angle and is 2.84.

where N_{sample} stands for the pole-pair number of rotating rectifier. N_{position} stands for the 12-bit digital signal of position.

As shown earlier, when load changes currently, the adaptive optimization method can change swiftly and reach a relatively lower value of phase current finally.

In the simulation, the adaptive optimization is applied to show the whole dynamic process of the weighted phase difference from the start. The advance angle values are changed to compare the phase current with that of the FSEW self-optimization control. The results are given in Figs. 11 and 13. Nonlinear inductance model is imported from MAXWELL and lookup method is used to build the nonlinear model.

The DSEM experiment platform is shown in Fig. 12. In experiment, Figs. 14–17 give the dynamic and steady performance. Although there exists a little fluctuation, but it is acceptable, considering the fluctuation of rotation speed.

In Fig. 17 (c) and (d), the ideal advanced angle appears closely after the point that the according torque can be generated, which is the same as the situation in simulation in Fig. 13. The results suit the analysis well. We know that phase difference increases as the advance angles increase. According to (10) or (14), that means $\cos\Delta\theta_{\mathrm{i}}$ decreases. To generate the output torque, I_{i} needs to be improved and thus ratio of torque to current decreases. So, the ideal advanced angle appears closely after the demanding

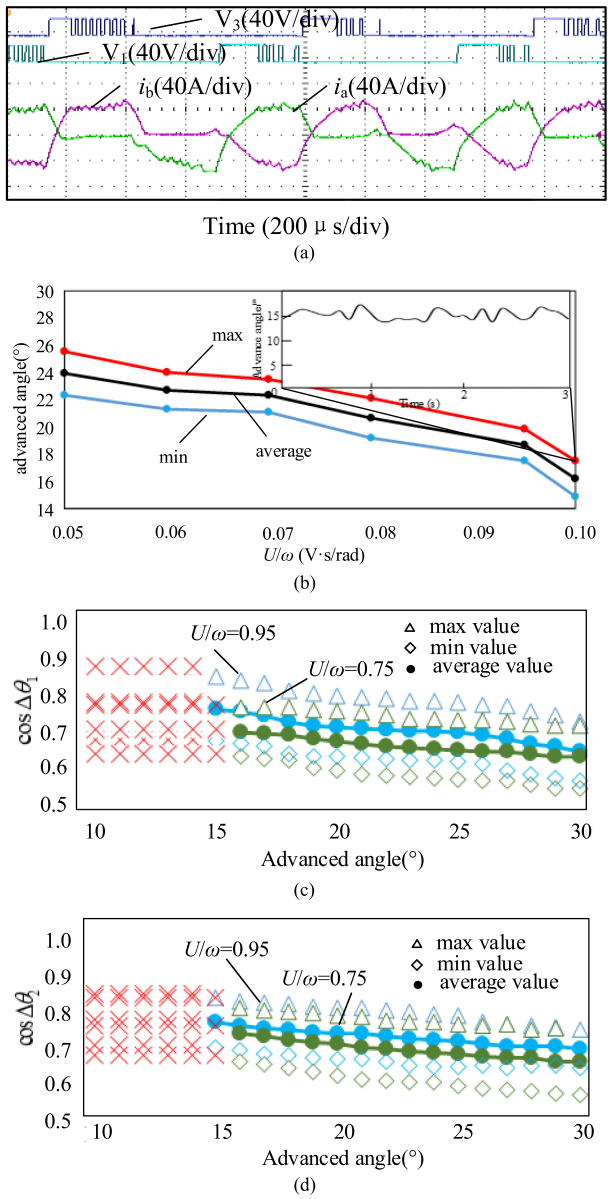

Fig. 17. Diagram of the phase current and digital signal of control under steady state (a) $n_{\mathrm{ref}} = 10\,000$ r/min, $U_{\mathrm{dc}} = 100$ V, $I_{\mathrm{f}} = 7$ A, and load $= 2$ kW: phase current under advance angle tuned by FSEW self-optimization method. (b) $U_{\mathrm{dc}} = 100$ V, $I_{\mathrm{f}} = 7$ A, and load $= 2$ kW: FSEW self-optimization results of advance angle. (c) Load $= 2$ kW. Phase difference of the first-order phase current obtained by harmonic detection. (Cross for the situation that according output torque cannot be generated). The three lines stand for the maximum value, average value and minimum value, respectively. (d) Load $= 2$ kW. Phase difference of the second-order phase current obtained by harmonic detection. (Cross for the situation that according output torque cannot be generated). The three lines stand for the maximum value, average value, and minimum value, respectively.

torque can be generated. However, quantitative calculation depends on the abovementioned analysis. By calculating the ration of torque to current, MTPA can be achieved.

VI. Conclusion

Aiming for improved accuracy of modeling and control, this article proposes a Fourier FEA model, a linear decoupled model, and an SFSC model. Then, by introducing the nth dq synchronous reference frame, a composite control strategy of hysteresis-six state advanced angle control-frequency shifted effect wighted (H-SAAC-FSEW) is proposed and MTPA control is realized. A related experiment is designed to verify the effectiveness of the abovementioned theories. Note that these models provide not only a self-optimization method to tune the AAC parameters, but also a quantitative model of the extremely nonlinear system. The following conclusion can be drawn.

1) In the time domain, a Fourier FEA model is proposed. This model reserves all the couplings. Based on that, a simple LDM is deduced, with the focus on the average output.
2) In the frequency domain, the SFSC model distinguishes the complex coupling between the torque and phase current. The transfer function of the average torque and third harmonic torque is deduced, and the frequency shift effect is proposed.
3) A composite self-optimization control strategy is proposed to achieve the MTPA by looking for the work point where the FSEW phase difference takes the maximum value.
4) A 3-D model of the excitation inductance is introduced here to explain the armature reaction on the proposed method. In ideal situation, the effect can be eliminated. Considering the saturation of magnetic materials, the effect still can be diminished.

References

[1] Y. Liao and T. A. Lipo, "A new doubly salient permanent magnet motor for adjustable speed drives," *Electric Mach. Power Syst.*, vol. 22, no. 2, pp. 259–270, 1994.
[2] Y. Liao, F. Liang, and T. A. Lipo, "A novel permanent motor with doubly salient structure," *IEEE Trans. Ind. Appl.*, vol. 31, no. 5, pp. 1069–1078, Sep./Oct. 1995.
[3] L. Durantay, N. Velly, J. F. Pradurat, and M. Chisholm, "New testing method for large high-speed induction motors," *IEEE Trans. Industry Appl.*, vol. 53, no. 1, pp. 660–666, Jan./Feb. 2017
[4] L. Yu, Z. Zhang, D. Gerada, and C. Gerada, "Performance comparison of doubly salient reluctance generators for high-voltage DC power system of more electric aircraft," in *Proc. IEEE Int. Conf. Elect. Syst. Aircr., Railway, Ship Propulsion Road Veh. Int.Transp. Electrific. Conf.*, Nottingham, U.K., 2018, pp. 1–6.
[5] F. Blaabjerg, L. Christensen, P. O. Rasmussen, L. Oestergaard, and P. Pedersen, "New advanced control methods for doubly salient permanent magnet motor," in *Proc. Conf. Rec. IEEE Industry Appl. Conf. 13th IAS Annu. Meeting*, vol. 1, Orlando, FL, USA, 1995, pp. 222–230.
[6] A. R. C. Sekhar Babu and K. R. Rajagopal, "FE analysis of multiphase doubly salient permanent magnet motors," *IEEE Trans. Magn.*, vol. 41, no. 10, pp. 3955–3957, Oct. 2005.
[7] X. D. Xue, K. W. E. Cheng, and S. L. Ho, "A self-training numerical method to calculate the magnetic characteristics for switched reluctance motor drives," *IEEE Trans. Magn.*, vol. 40, no. 2, pp. 734–737, Mar. 2004.
[8] X. D. Xue, K. W. E. Cheng, S. L. Ho, and K. F. Kwok, "Trigonometry-based numerical method to compute nonlinear magnetic characteristics in switched reluctance motors," *IEEE Trans. Magn.*, vol. 43, no. 4, pp. 1845–1848, Apr. 2007.
[9] L. Zhang, B. Zhou, F. Cheng, and Y. Zhang, "Modeling and dynamic simulation of a novel doubly salient electro-magnetic wind power generator system," in *Proc. World Non-Grid-Connected Wind Power and Energy Conf.*, Nanjing, China, 2009, pp. 1–6.
[10] E. C. Sagiroglu *et al.*, "Modeling of a nonlinear switched reluctance driver based on artificial neural networks," in *Proc. 5th Int. Conf. Power Electron. Variable Speed Drives*, London, U.K., pp. 7–12, 1994.

[11] J. S. Jang, "ANFIS adaptive-network-based fuzzy inference systems," *IEEE Trans. Syst. Man Cybern.*, vol. 23, no. 3, pp. 665–685, May/Jun. 1993.
[12] T. Tagaki and M. Sugeno, "Fuzzy identification of systems and its applications to modeling and control," *IEEE Trans. Syst. Man Cybern.*, vol. 15, no. 1, pp. 116–132, Jan./Feb. 1985.
[13] Q. Hu and Y. Yan, "Prior angle control for doubly salient permanent magnet motor," *Trans. China Electrotech. Soc.*, vol. 20, no. 9, pp. 13–18, 2005.
[14] X. Zhu, M. Cheng, W. Zhao, and W. Li, "Advanced angle control schemes for stator hybrid excited doubly salient motor drive," in *Proc. CES/IEEE 5th Int. Power Electron. Motion Control Conf.*, Shanghai, China, 2006, pp. 1–5.
[15] X. Zhou, B. Zhou, and L. Yang, "Self-optimizing control of advanced commutation angle for doubly salient electromagnetic machine," in *Proc. IECON - 43rd Annu. Conf. IEEE Ind. Electron. Soc.*, 2017, pp. 4403–4407.
[16] W. Yuan, Y. Wang, Z. Zhang, and R. Liang, "Torque ripple suppression of doubly salient brushless DC motors with current compensation control," *Proc. IEEE 8th Int. Power Electron. Motion Control Conf.*, Hefei, China, 2016, pp. 2831–2836.
[17] C. Ma, B. Zhou, and L. Zhang, "Study on new speed control system for doubly salient permanent magnet motor," *Proc. CSEE*, vol. 27, no. 9, pp. 71–76, 2007.
[18] W. Jia and L. Xiao, "Research on control strategies for doubly salient electromagnetic machine," *IET Electric Power Appl.*, vol. 11, no. 8, pp. 1449–1456, Sep. 2017.
[19] Z. Bian, Z. Zhang, and L. Yu, "Synchronous commutation control of doubly salient motor drive with adaptive angle optimization," *IEEE Trans. Power Electron.*, to be published, doi: 10.1109/TPEL.2019.2949095.
[20] L. Zhang, B. Zhou, F. Cheng, and Y. Zhang, "Modeling and dynamic simulation of a novel doubly salient electro-magnetic wind power generator system," *World Non-Grid-Connected Wind Power Energy Conf*, Nanjing, China, 2009, pp. 1–6.

Yinfeng Hu was born in Chongqing, China in 1996. He received the bachelor's degree in electrical engineering from Huazhong University of Science and Technology, Wuhan, China, in 2018. He is currently working toward the Master's degree with Nanjing University of Aeronautics and Astronautics, Nanjing, China.

His research interests include power electronics and motor drive.

Lan Xiao (Member, IEEE) was born in Zhejiang, China, in 1971. She received the B.S. and Ph.D. degrees in electrical engineering from Nanjing University of Aeronautics and Astronautics (NUAA), Nanjing, China, in 1993 and 1998, respectively.

In 1999, she joined the Faculty of the College of Automation Engineering, NUAA, where she is currently a Professor of New Energy Generation and Power Conversion with Jiangsu Key Laboratory. She is the author or co-author of more than 60 technical papers published in journals and conference proceedings. Her research interests include soft-switching dc/dc converters, soft-switching inverters, and renewable energy generation systems.

Chen Pan was born in Hubei, China in 1996. She received the bachelor's degree in electrical engineering in 2018 from the Huazhong University of Science and Technology (HUST), Wuhan, China, where she is currently working toward the master's degree in applied electronic engineering.

His research interests include power electronics and power transmission.

Jinbo Li (Student Member, IEEE) received the B.S degree from Beijing Jiaotong University, Beijing, China, in 2010, and the M.S. degree from Ningxia University, Yinchuan, China, in 2016. He is currently working toward the Ph.D. degree with the College of Automation Engineering, Nanjing University of Aeronautics and Astronautics, Nanjing, China.

From 2010 to 2014, he was an Electrical Engineer with a hydropower plant. His research interests include grid synchronization, digital filter, and grid stability.

Chuyang Wang was born in Jiangsu, China, in 1990. He received the B.S. and Ph.D. degrees in electrical engineering from the Nanjing University of Aeronautics and Astronautics (NUAA), Nanjing, China, in 2012 and 2019, respectively.

In 2019, he joined the Faculty of Electrical Engineering, Hohai University, Nanjing, China, where he is currently a lecturer. His current research interests include modular multilevel converters, new energy power generation, and digital control applied to power electronics.